NSRRC-Jo4460 (2014)

THE JOURNAL OF PHYSICAL CHEMISTRY C

Article

pubs.acs.org/JPCC

Control of Nanostructural Dimension by Crystallization in a Double-Crystalline Syndiotactic Poly(4-methyl-1-pentene)-*block*-poly(L-lactide) Block Copolymer

Yeo-Wan Chiang,*[,†] You-Wei Huang,[†] Shih-Hung Huang,[†] Pei-Sun Huang,[‡] Yung-Cheng Mao,[‡] Chih-Kuang Tsai,[‡] Chin-Shuo Kang,[‡] Jing-Cherng Tasi,[‡] Chun-Jen Su,[§] U-Ser Jeng,[§,∥] and Wen-Hsien Tseng[⊥]

[†]Department of Materials and Optoelectronic Science, Center for Nanoscience and Nanotechnology, National Sun Yat-Sen University, Kaohsiung 80424, Taiwan

[‡]Department of Chemical Engineering, National Chung Cheng University, Chia-Yi 62142, Taiwan

[§]National Synchrotron Radiation Research Center, Hsinchu 30076, Taiwan

[∥]Department of Chemical Engineering, National Tsing Hua University, Hsinchu 30013, Taiwan

[⊥]AU Optronics Technology Center, AU Optronics Corporation, Hsinchu 30078, Taiwan

S *Supporting Information*

ABSTRACT: The control of nanostructural dimension by crystallization-induced chain stretching was investigated in a novel double-crystalline block copolymer, syndiotactic poly(4-methyl-1-pentene)-*block*-poly(L-lactide) (*s*PMP–PLLA), featuring a lamellar phase. Because of the similar glass transition temperatures of *s*PMP and PLLA, their blocks could crystallize under soft confinement (i.e., a crystallization temperature higher than the glass transition temperatures of the constituent blocks) in *s*PMP–PLLA. With the strong segregation of *s*PMP–PLLA, the first-crystallized *s*PMP block was templated by microphase separation to form confined crystalline *s*PMP lamellae within the microphase-separated lamellar texture. Most interestingly, the first-crystallized *s*PMP block may also induce significant stretching of the PLLA chains from the lamellar interface, resulting in the increase of microdomain thickness of the PLLA block. With the increase of crystallization temperature, this chain stretching may become more significant, resulting in a large increase (~34%) of the lamellar long period. The double-crystalline lamellar morphologies having homeotropic orientation for both *s*PMP and PLLA crystals can be acquired in the shear-aligned *s*PMP–PLLA as evidenced by simultaneous 2D small-angle X-ray scattering and wide-angle X-ray diffraction, giving uniform birefringence under polarized light microscope with thermal reversibility. As a result, the switchable lamellar nanostructures having significant dimensional change can be carried out by simply controlling crystallization or melting of the crystallizable blocks.

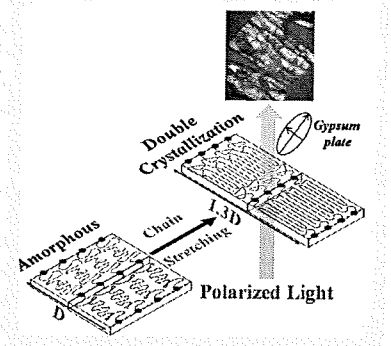

INTRODUCTION

Block copolymers (BCPs) having different ordered nanostructures, such as body-centered cubic spheres, hexagonally packed cylinders, gyroids, and lamellae, are promising for practical applications.[1,2] Since the microphase-separated morphologies of BCPs and their dimensions are inevitably affected by the crystallization of crystallizable blocks, the investigation on mutual interactions between microphase separation and crystallization has drawn intensive attention in recent years. For crystallization in semicrystalline BCPs, various crystalline morphologies, such as confined, breakout, template, and undulated textures, were strongly dependent on the order–disorder transition temperature (T_{ODT}), the crystallization temperature of the crystalline block (T_c), and the glass transition temperature of the amorphous block (T_g).[3−27] While $T_c^c > T_{ODT}$, the crystallization occurs before the microphase separation of BCP, resulting in breakout morphology.[6,24] While $T_{ODT} > T_c^c > T_g^a$, the crystallization is carried out within mobile microphase-separated texture (i.e., soft confinement), giving breakout or undulated morphologies according to the segregation strength of BCP.[6,24] While $T_{ODT} > T_g^a > T_c^c$, the crystallization performs within vitrified microphase-separated structure (i.e., hard confinement), resulting in confined morphology.[19,20,22,25] Namely, the final morphologies of semicrystalline BCPs are the consequence of the segregation strength, crystallization, and vitrification.

In contrast, double-crystalline BCPs (that is, crystalline–crystalline BCPs) may exhibit much more complicated crystalline behaviors than the semicrystalline BCPs due to the further effect from crystallization sequence.[28,29] For a double-

Received: May 20, 2014
Revised: July 22, 2014
Published: July 29, 2014

ACS Publications © 2014 American Chemical Society

dx.doi.org/10.1021/jp504976s | J. Phys. Chem. C 2014, 118, 19402−19414

crystalline BCP, double crystallization can be carried out by two-stage isothermal crystallization in sequence as the crystallization temperature for one of the crystalline blocks is quite different from the other.[30−43] In analogy to semicrystalline BCPs, the first-crystallized (i.e., single-crystalline) morphology in the double-crystalline BCP is mainly determined by the segregation strength, crystallization, and vitrification. Notably, the final morphology will be directed by the earlier established crystalline morphology as a structural template. According to the mechanical strength of the template, various final morphologies are found. For a robust crystalline template, invariant morphology similar to the first-crystallized morphology is found.[32−36,39−43] In contrast, for a shaky crystalline template, the subsequent crystallization may overwhelm the established crystalline morphology, causing a morphological transition.[33,34,38] Accordingly, the double-crystalline morphologies are mainly dependent on the crystallization sequence. In contrast to the two-stage crystallization, if crystallization temperatures for the two crystallizable blocks are similar, double crystallization can be accomplished by one-stage isothermal crystallization.[41,44−52] As a result, the final morphologies are more complicated due to the interactive consequence of the microphase separation, crystallization, vitrification, and crystalline sequence. The double-crystalline BCPs are promising in the design of optical materials with tunable birefringence.

In this study, crystallization behavior of a novel double-crystalline BCP, syndiotactic poly(4-methyl-1-pentene)-*block*-poly(L-lactide) (*s*PMP−PLLA) featuring a lamellae-forming phase, was examined. Notably, *s*PMP and PLLA blocks can crystallize under soft confinement in the *s*PMP−PLLA BCP due to the same values of T_g. Owing to similar crystallization temperature, the double crystallization can be accomplished by one-stage isothermal crystallization. With the strong segregation of *s*PMP−PLLA, the first-crystallized *s*PMP was templated by BCP microphase separation to form crystalline *s*PMP lamellae within microphase-separated lamellar texture. The following PLLA crystallization was thus strongly confined by the robust crystalline *s*PMP lamellae. Significant stretching of the PLLA chains in the *s*PMP−PLLA BCP is driven by the first-crystallized *s*PMP, resulting in the increase of the microdomain thickness of the PLLA block. Also, the final morphology of the shear-aligned *s*PMP−PLLA after double crystallization exhibits the lamellar nanostructure with homeotropic orientation for both *s*PMP and PLLA crystals, leading to uniform birefringence with thermal reversibility.

EXPERIMENTAL SECTION

Materials and Sample Preparation. The PLLA homopolymer[53] and the *s*PMP homopolymer[54] were prepared by methods described in the literature. The *s*PMP−PLLA was prepared in two steps. First, hydroxyl-capped *s*PMP was synthesized by syndiospecific polymerization of 4-methyl-1-pentene conducted in the presence of triethylaluminum (chain transfer agent) using $Me_2C(Cp)(Flu)ZrCl_2$/MAO as a catalyst.[55−57] The resulting aluminum-capped *s*PMP was in situ treated with O_2/H_2O to provide the hydroxyl-capped *s*PMP. Second, the *s*PMP−PLLA was synthesized by ring-opening polymerization of L-lactide using tin(II) octoate as the catalyst and hydroxyl-capped *s*PMP as the macroinitiator. The detailed synthetic procedures for the generation of *s*PMP−PLLA will be reported in another paper. The molecular weight and composition of the *s*PMP−PLLA were determined by gel permission chromatography (GPC) and nuclear magnetic resonance (NMR). The volume fraction of the PLLA block is estimated by assuming that the densities of *s*PMP and PLLA are 0.84 and 1.25 g/cm^3, respectively. The samples are listed in Table 1.

Table 1. Characterization of the Homopolymers and Block Copolymer

sample	$M_{n,sPMP}$ (g/mol)	$M_{n,PLLA}$ (g/mol)	$M_{n,total}$ (g/mol)	f_{PLLA}	PDI
*s*PMP−PLLA	9800	13200	23000	0.48	1.11
*s*PMP	10100				1.20
PLLA		11500			1.21

Bulk samples of the *s*PMP−PLLA block copolymers were prepared by solution casting from dichloromethane solution (5 wt %) at room temperature for 2 weeks. The bulk samples were then dried in a vacuum oven for 3 days to remove the residual solvents.

Differential Scanning Calorimetry (DSC). The samples were first heated to the temperature of microphase-separated melt at 210 °C for 3 min to eliminate the thermal history from casting using a PerkinElmer DSC7 equipped with an Intracooler II. For experiments with nonisothermal crystallization, the samples were first heated to 210 °C for 3 min and then cooled to −50 °C at a rate of 10 °C/min. For experiments with isothermal crystallization, the samples were first heated to 210 °C for 3 min and then rapidly cooled at a rate of 150 °C/min to the preset crystallization temperature, T_c. The melting temperature, T_m, of each sample was recorded by a scan rate of 10 °C/min in DSC. The melting temperatures and endotherms at different heating rates were carefully calibrated using standard materials. Each of the sample weights was 5 mg in all treatments of DSC.

Transmission Electron Microscopy (TEM). Bulk samples of the *s*PMP−PLLA was microtomed at room temperature for transmission electron microscopic (TEM) observation. A Reicher Ulracut microtome equipped with a diamond knife was utilized for ultramicrosection. Staining was accomplished by exposing the microsections to the vapor of a 4% aqueous RuO_4 solution for 2 h. Bright field TEM images of mass−thickness contrast were obtained from the stained microsections on a JEOL JEM-2100 TEM, at an accelerating voltage of 200 kV. After staining by RuO_4 vapor, *s*PMP microdomains appear bright and the PLLA microdomains appear dark due to the enhanced difference of the mass−thickness contrast.

X-ray Experiments. Simultaneous small-angle X-ray scattering (SAXS) and wide-angle X-ray diffraction (WAXD) experiments were conducted at the synchrotron X-ray beamline 23A at the National Synchrotron Research Center (NSRRC) in Taiwan.[58] The wavelength λ of the X-ray beam was 0.2066 nm. A MAR CCD X-ray detector (MAR USA) was used for collecting the two-dimensional (2D) SAXS patterns. One-dimensional (1D) SAXS profiles were obtained by azimuthal integration of the 2D SAXS patterns. The scattering angle of the SAXS pattern was calibrated using silver behenate, with the first-order scattering vector $q^* = 1.076$ nm^{-1} ($q^* = 4\pi\lambda^{-1} \sin\theta$, where 2θ is the scattering angle).

RESULTS AND DISCUSSION

Characterization of Double-Crystalline *s*PMP−PLLA BCP. The thermal behavior of the *s*PMP−PLLA BCP, the

dx.doi.org/10.1021/jp504976s | J. Phys. Chem. C 2014, 118, 19402−19414

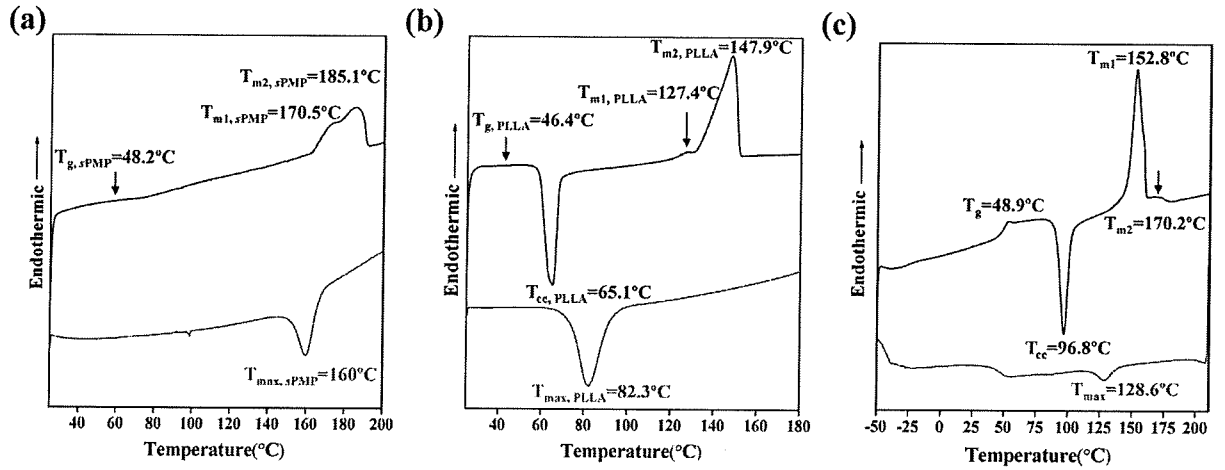

Figure 1. DSC cooling (lower) and heating (upper) curves for the (a) *s*PMP homopolymer, (b) PLLA homopolymer, and (c) *s*PMP–PLLA BCP. The samples for heating examinations were preliminarily quenched from the melt. Scan rates: 10 °C/min.

*s*PMP homopolymer, and the PLLA homopolymer were investigated using DSC. The DSC thermograms in Figures 1a and 1b reveal that the glass transition temperatures of the *s*PMP homopolymer ($T_{g,sPMP}$) and the PLLA homopolymer ($T_{g,PLLA}$) were 48.2 and 46.4 °C (see Figure S1 for high magnification), respectively; that is, these homopolymers possess the same values of T_g.[59,60] The melting temperature of the *s*PMP homopolymer ($T_{m,sPMP}$ = 170–185 °C) is, however, higher than that of the PLLA homopolymer ($T_{m,PLLA}$ = 127–148 °C); in addition, the temperature of the maximum crystallization rate of the *s*PMP homopolymer ($T_{max,sPMP}$ = 160.0 °C) is also higher than that of the PLLA homopolymer ($T_{max,PLLA}$ = 82.3 °C). Notably, in contrast to a cold crystallization temperature for the PLLA homopolymer ($T_{cc,PLLA}$) of 65.1 °C, no further crystallization of the *s*PMP homopolymer occurred during the second heating scan, due to its complete crystallization upon cooling. For the *s*PMP–PLLA BCP, a single value of T_g is identified near 48.9 °C (Figure 1c), a value of T_{cc} of 96.8 °C, and two melting peaks: a large endothermic peak (T_{m1}) at 152.8 °C and a small endothermic peak (T_{m2}) at 170.2 °C. Corresponding WAXD data (not shown here) for this *s*PMP–PLLA sample revealed the characteristic reflections of both the *s*PMP and PLLA crystalline structures, suggesting that the two endothermic peaks can be attributed to the melting of *s*PMP and PLLA crystallites, respectively. As a result of the similar values of T_g for *s*PMP and PLLA, the double-crystalline *s*PMP–PLLA BCP might exhibit unique crystallization behavior, with both the *s*PMP and PLLA blocks being crystallized under soft confinement. In contrast to the characteristics of the *s*PMP homopolymer, the value of T_{max} for the *s*PMP–PLLA BCP under cooling decreased significantly (to 128.6 °C) and an obvious cold crystallization was evident (at 96.8 °C), further demonstrating the effect of confined behavior on the crystallization properties.

To further examine the crystallization behavior of the *s*PMP–PLLA BCP, isothermal crystallization was conducted. First, all samples were heated at 210 °C for 3 min to erase the thermal history from solution casting and then were rapidly cooled (150 °C/min) to a preset temperature (T_c) for isothermal crystallization. The DSC thermograms feature two distinct exothermic peaks during isothermal crystallization at values of T_c ranging from 80 to 120 °C (Figure 2a). For

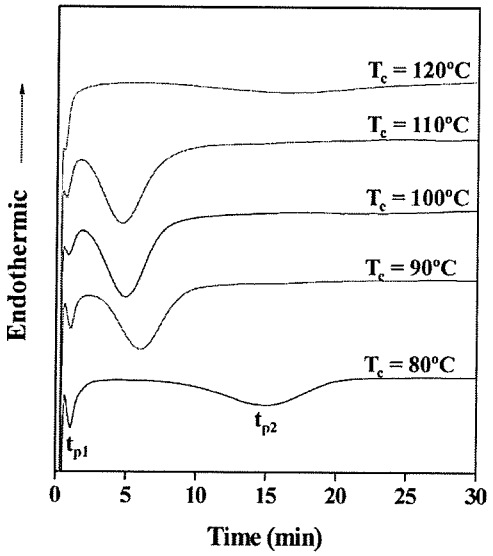

Figure 2. DSC thermograms of the *s*PMP–PLLA BCP crystallized isothermally at various temperatures.

instance, at a value of T_c of 90 °C, a small exothermic peak appeared at 1 min (denoted "t_{p1}") and a large exothermic peak appeared at approximately 6 min (denoted "t_{p2}"), indicating that two crystallization events occurred in sequence. To further examine these sequential crystallization events, WAXD experiments were conducted using *s*PMP–PLLA samples isothermally crystallized for different periods of time. First, a bulk sample of the *s*PMP–PLLA BCP was isothermally crystallized at 90 °C for 3 min ($t_{p1} < t < t_{p2}$) and was then quenched into liquid N_2 to acquire a sample from the first crystallization event. The WAXD data in Figure 3a suggest that the *s*PMP block crystallized first, as evidenced by the appearance of the (200) and (217) reflections of the crystalline *s*PMP structure (denoted "$(200)_{sPMP}$" and "$(217)_{sPMP}$," respectively). In contrast, after isothermal crystallization at 90 °C for 60 min ($t \gg t_{p2}$), the corresponding WAXD profile reveals the characteristic reflections of both crystalline *s*PMP and PLLA structures (Figure 3b); that is, double crystallization had

dx.doi.org/10.1021/jp504976s | J. Phys. Chem. C 2014, 118, 19402–19414

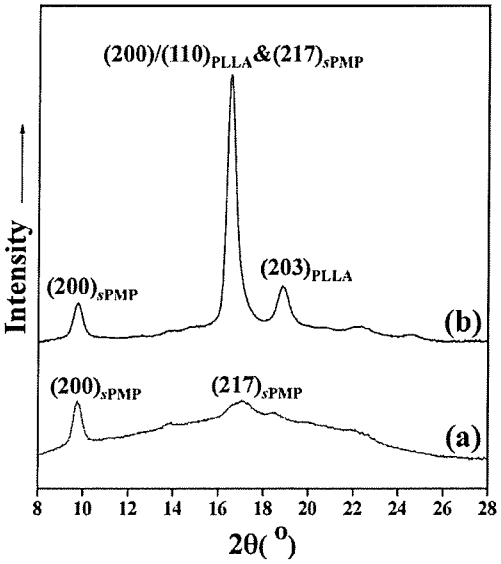

Figure 3. WAXD profiles of the *s*PMP–PLLA BCP after isothermal crystallization at 90 °C for (a) 3 and (b) 60 min.

occurred. Accordingly, the second crystallization event is attributed to crystallization of the PLLA block. Similar results were obtained when the sample crystallized at different temperatures. In addition, on the basis of the integrated areas of the exothermic peaks and the heats of melting (Figure 2), we believe that the crystallinity of the crystallized PLLA block was higher than that of the crystallized *s*PMP block after double crystallization.

Effect of Sequential Crystallization on Microphase-Separated Morphology. The morphologies of the microphase-separated *s*PMP–PLLA BCP were examined using TEM and SAXS. Figure 4a reveals ordered layer structures for the *s*PMP–PLLA BCP after its quenching from the ordered melt, indicating the formation of microphase-separated lamellae. The 1D SAXS profile displays intense reflections at the relative q values of 1:2:3:4:5 (Figure 4b), further confirming the formation of a well-ordered lamellar phase. The corresponding WAXD data reveal a typical amorphous profile (Figure 4c), indicating that no crystallization occurred in the *s*PMP–PLLA BCP after quenching from the melt. The lamellar phase exhibited a long period of 32 nm, determined from the primary reflection of the SAXS profile. To resolve the thicknesses of the *s*PMP (d_{sPMP}) and PLLA (d_{PLLA}) microdomains, we applied the normalized 1D correlation function to the SAXS data. The normalized 1D correlation function $[\gamma(z)]$ can be obtained using the equation[61,62]

$$\gamma(z) = \frac{1}{Q}\int_0^\infty q^2 I(q)\cos(qz)\,dq$$

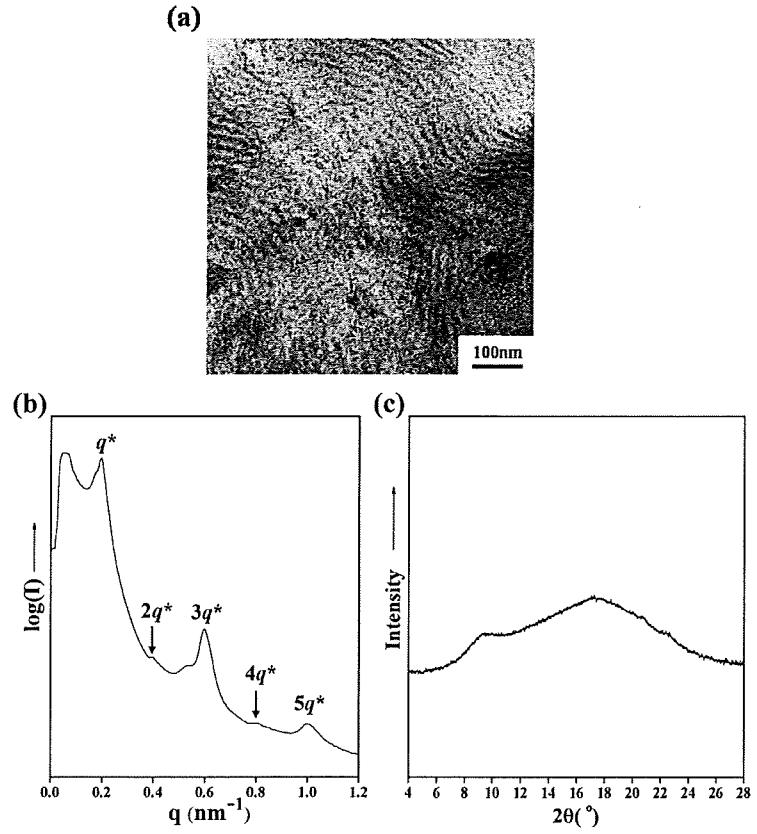

Figure 4. (a) TEM micrograph and (b) SAXS and (c) corresponding WAXD profiles of the *s*PMP–PLLA BCP after quenching from the melt at 210 °C. With RuO_4 staining, the dark region is PLLA and bright area is *s*PMP.

where z is the coordinate along the electron density distribution, q is the scattering vector, $I(q)$ is the observed 1D intensity, and the invariant Q is the integrated scattering intensity with respect to q, defined by

$$Q = \int_0^\infty q^2 I(q)\, dq$$

First, thermal fluctuations were subtracted from the observed scattering intensity by evaluating the slopes of plots of $I(q)q^4$ versus q^4 at wide scattering vectors q, so as to fit the 1D correlation function. Accordingly, the correlation function $[\gamma(z)]$ which varied with respect to the real space coordinate (z) was plotted using the normalized 1D correlation function. The characteristic spacing for the thinner layer from the intercept (for the real space coordinate axis) was calculated from the tangent line near the position at $z = 0$. Figure 5 reveals

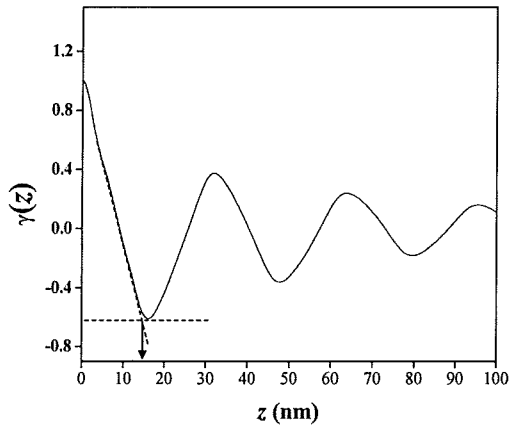

Figure 5. Normalized 1D correlation function for the *s*PMP–PLLA BCP after quenching from the melt at 210 °C. The thickness of lamellar long period was calculated from the position of first peak; the average thickness of the thinner layer was determined from the crossover point of the tangent and baseline of the first wave trough.

that the thinner spacing and the long period were 15.2 and 32 nm, respectively. As calculated, the volume fraction of PLLA blocks in the *s*PMP–PLLA BCP was 0.48. Therefore, the thinner spacing is defined as d_{PLLA}, which is in line with the result calculated from the BCP composition (long period × f_{PLLA}^{v} = 32 × 0.48 = 15.4 nm). Detailed quantitative information about long periods and microdomain thickness of the *s*PMP–PLLA under various thermal treatments is summarized in Table 2.

To investigate the effect of sequential crystallization on the microphase-separated lamellar phase in the *s*PMP–PLLA BCP, isothermally crystallized samples for different periods of time were prepared. At 210 °C, the SAXS profile exhibits sharp and intense reflections at relative q values of 1:3 (Figure 6a), suggesting the formation of a microphase-separated lamellar phase; in other words, the order–disorder transition temperature (T_{ODT}) of the *s*PMP–PLLA BCP should be above 210 °C. On the basis of the primary reflection in the SAXS data, the long period of the microphase-separated lamellar phase at 210 °C was calculated to be 24.8 nm. For the crystallization experiments, we first heated each sample at 210 °C for 3 min, rapidly cooled it to a preset temperature for crystallization, and finally quenched it to 25 °C (a temperature far below the values of both $T_{g,PLLA}$ and $T_{g,sPMP}$) to preserve its crystallized morphology. After crystallization at T_c = 90 °C for 3 min, the lamellar morphology remains without any significant effect of the crystallization event (Figure 6b). Consistently, the reflections in the SAXS profile occurred at relative q values of 1:3 but shifted to the lower-q region—revealing the preservation of the lamellar phase, but with larger long period. In addition, no spherulite texture was observed under polarized light microscopy (PLM), suggesting confined crystallization (Figure S2). Accordingly, the first crystallization of *s*PMP occurred within the microphase-separated lamellae to form crystalline lamellae having a larger microdomain, which is attributed to crystallization-induced thickening of the microdomains (see below for further discussion). The preservation of the microphase-separated lamellar phase is attributed to the strong segregation of the *s*PMP–PLLA BCP. This can be expected from the data of solubility parameters (δ), which exhibit a large difference between δ_{sPMP} [7.6 = $(cal/cm^3)^{1/2}$] and δ_{PLLA} [10.9 = $(cal/cm^3)^{1/2}$].[63,64]

Upon increasing the crystallization time for isothermal crystallization at 90 °C to, for example, 60 min, the 1D SAXS profile remains unchanged (Figure 6a). Namely, the subsequent PLLA crystallization process did not alter the dimensions of the lamellar structure. This phenomenon was further evidenced by the observation of a lamellar morphology under TEM (Figure 6c) and by the absence of any spherulitic texture under PLM (Figure S3). Consequently, the first-crystallized *s*PMP block created a robust crystalline template similar to hard confinement for the subsequent PLLA crystallization, giving a lamellar morphology having an invariant long period after double crystallization.

To further explore the relationship between crystallization and microphase separation, time-resolved simultaneous SAXS and WAXD experiments were performed. The SAXS data in Figures 7a and 7b reveal a microphase-separated lamellar phase with the relative q values of 1:3 for the *s*PMP–PLLA BCP rapidly cooled from the melt to 90 °C (t = 0). In addition, no significant reflection in the corresponding WAXD profile indicated that the rapidly cooled sample is in an amorphous state (Figure 7c). After crystallization at 90 °C for 1 min, two sets of lamellar reflections could be identified (Figures 7a and 7b). In addition to the reflections at the q values of 0.209 and

Table 2. Long Periods and Microdomain Thicknesses of the *s*PMP–PLLA

	quench from melt	at 210 °C	T_c = 90 °C for 0 min	T_c = 90 °C for 3 min	T_c = 90 °C for 30 min	T_c = 110 °C for 0 min	T_c = 110 °C for 1 min	T_c = 110 °C for 30 min
long period[a] (d) (nm)	32	24.8	30	37.0	37.2	28.8	38.3	38.5
*s*PMP thickness[a] (d_{sPMP}) (nm)	16.8	13.2	16.1	19.4	19.7	15.5	20.7	20.8
PLLA thickness[a] (d_{PLLA}) (nm)	15.2	11.6	13.9	17.6	17.5	13.5	17.6	17.7

[a]Determined by normalized 1D correlation function.

dx.doi.org/10.1021/jp504976s | J. Phys. Chem. C 2014, 118, 19402–19414

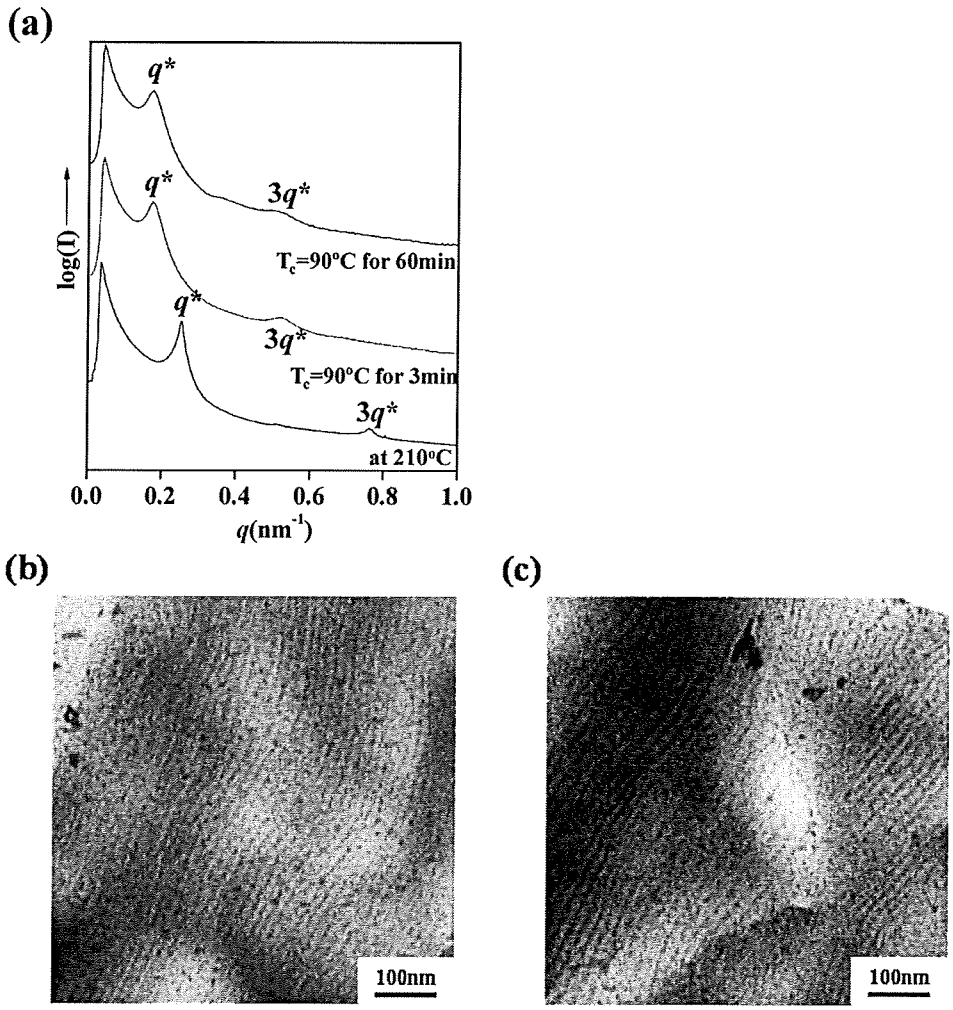

Figure 6. (a) SAXS profiles for the *s*PMP–PLLA BCP at 210 °C and after isothermal crystallization at 90 °C for 3 and 60 min. (b, c) TEM micrographs of the *s*PMP–PLLA BCP crystallized at 90 °C for (b) 3 and (c) 60 min.

0.627 nm^{-1} from the amorphous lamellar phase, new scattering peaks were observed at the lower values of q of 0.169 and 0.512 nm^{-1} with relative q values of 1:3 (see arrows in Figure 7b), indicating the formation of a new lamellar phase having a larger long period. The corresponding WAXD profile with the $(200)_{sPMP}$ reflection at 9.8° suggests that the new lamellar structure is attributed to the crystallization of *s*PMP (Figure 7c). Upon increasing the crystallization time to 2 min, the scattering intensity from the *s*PMP crystallization event increased significantly, while the intensity from the original amorphous lamellae decreased dramatically (Figure 7b). Further increasing the crystallization time to 3 min caused the scattering from the amorphous lamellae to disappear completely—only scattering from the *s*PMP crystallization event was observed, revealing a complete phase transition from the amorphous lamellae to the crystalline *s*PMP lamellae. Notably, the time period corresponds well with the development of the relative crystallinity of the *s*PMP block ($X_{r,sPMP}$), which reached its maximum after 3 min (Figure 8a). Here, we define the relative crystallinity (X_r) as the ratio of the integrated area of the reflection at a given time to the integrated area of the reflection from the saturated crystallization ($X_r = A^t/A^\infty$). Accordingly, the increase in the value of $X_{r,sPMP}$ upon increasing the crystallization time may give rise simultaneously to the enhanced scattering intensity for the *s*PMP crystalline lamellae. As a result, the first-crystallized *s*PMP may drive the amorphous microphase-separated lamellae to form crystalline *s*PMP lamellae having a larger long period.

Following the *s*PMP crystallization event, the PLLA block crystallized subsequently, as evidenced by the appearance of $(200)_{PLLA}/(110)_{PLLA}$ reflections at 16.5° after isothermal crystallization at 90 °C for 5 min (Figure 7c). Figure 8a reveals that the relative crystallinity of the PLLA block ($X_{r,PLLA}$) reached a maximum after 14 min, indicating its complete crystallization. The 1D SAXS profiles remained almost unchanged, however, after isothermal crystallization for 3 min, indicating that the subsequent PLLA crystallization was confined strongly within the first-crystallized *s*PMP lamellae. Consequently, the self-assembled morphology after crystallization at 90 °C was mainly dominated by the first-crystallized *s*PMP, regardless of subsequent PLLA crystallization.

Figure 8b displays the time-resolved long period and the respective microdomain thickness in the *s*PMP–PLLA BCP at T_c = 90 °C, acquired using the normalized 1D correlation

dx.doi.org/10.1021/jp504976s | J. Phys. Chem. C 2014, 118, 19402–19414

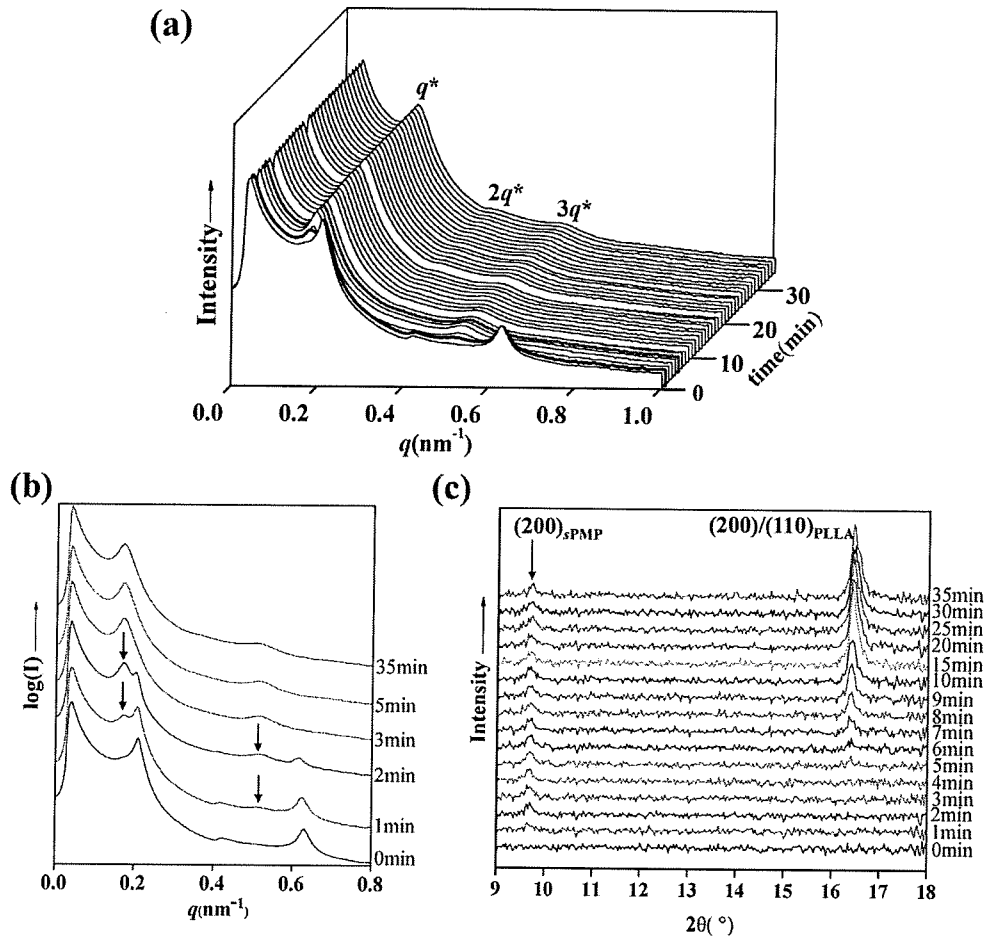

Figure 7. Time-resolved (a) SAXS, (b) 1D SAXS, and (c) WAXD profiles of the *s*PMP–PLLA BCP crystallized isothermally at 90 °C.

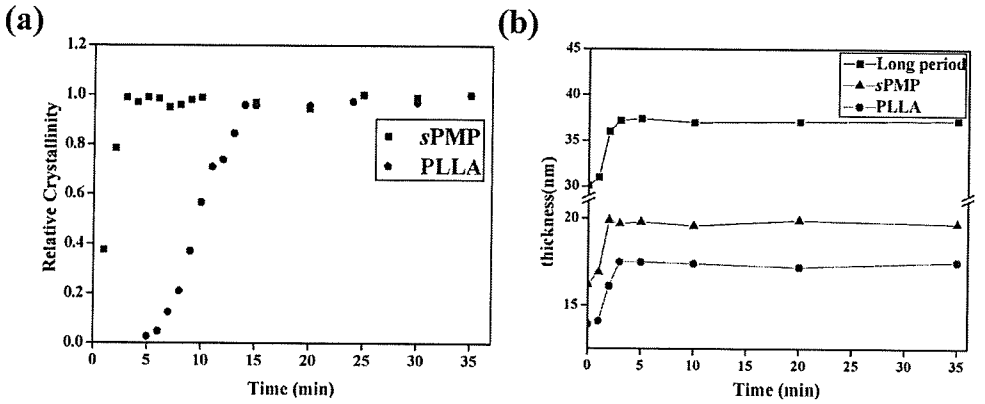

Figure 8. (a) Relative crystallinity of the respective *s*PMP and PLLA blocks plotted with respect to the isothermal annealing time, determined from time-resolved WAXD profiles recorded at T_c = 90 °C. (b) Time-dependent long periods and respective microdomain thicknesses of the *s*PMP and PLLA blocks, determined from time-resolved SAXS profiles recorded at T_c = 90 °C.

function. As the *s*PMP block crystallized within 3 min, a significant increase in its microdomain thickness was observed. We suggest that dense packing of the *s*PMP chains in a crystalline unit cell may result in shrinkage of the junction distance on the lamellar interface, leading to stretching of the *s*PMP chains and an increase in the microdomain thickness of the *s*PMP (i.e., crystallization-induced thickening of microdomains). Meanwhile, the microdomain thickness of the PLLA also increased dramatically within 3 min (Figure 8b); because the crystallization of PLLA still had not occurred at this period of time, it is reasonable to suggest that the constituted PLLA chains were stretched as a result of the shrinkage of the junction

dx.doi.org/10.1021/jp504976s | J. Phys. Chem. C 2014, 118, 19402–19414

distance. This phenomenon may have resulted in the increase in the microdomain thickness of PLLA, namely, chain stretching of the PLLA driven by the first-crystallized *s*PMP. As calculated, the long period was 37.2 nm for the *s*PMP–PLLA BCP crystallized isothermally at 90 °C for 3 min—an increase of 24% relative to that (30.0 nm) of the amorphous microphase-separated lamellae. Figure S4 shows the SAXS profiles for the *s*PMP and PLLA homopolymers under the similar crystalline conditions. The long periods of the *s*PMP and PLLA homopolymer are always smaller than the thicknesses of the *s*PMP and PLLA microdomains in the *s*PMP–PLLA under the similar crystalline conditions (see Table S1), further demonstrating the chain stretching behavior. In contrast, the long period and the microdomain thicknesses remained almost constant as the period of time ≥3 min, even though the PLLA had yet to be subsequently crystallized (Figure 8b). As a result, this finding clearly indicates that the PLLA chains were indeed stretched by the first-crystallized *s*PMP and that the subsequent PLLA crystallization event was strongly confined within the robust *s*PMP crystalline lamellae.

We also examined the self-assembled morphologies and their dimensional changes of the *s*PMP–PLLA BCP crystallized isothermally at higher crystallization temperatures (e.g., T_c = 110 °C; Figure S5). Similar to the phase structures obtained at T_c = 90 °C, two sets of lamellar reflections, including those for amorphous lamellae (at q values of 0.218, 0.433, and 0.648 nm^{-1}) and those for *s*PMP crystalline lamellae (at q values of 0.163, 0.329, and 0.492 nm^{-1}), were evident after t = 1 min (Figure S5b), as evidenced by the appearance of the $(200)_{sPMP}$ in the corresponding WAXD profiles (Figure S5c). Upon increasing the crystallization time to 2 min, a complete phase transition from the amorphous lamellae to the *s*PMP crystalline lamellae was observed. Again, because the time period for the phase transition was identical to that for the maximum value of $X_{r,sPMP}$ (Figure S6a), the phase transition was driven mainly by the first-crystallized *s*PMP. Notably, the time period of the phase transition at T_c = 110 °C was reduced as comparison with that at 90 °C, due to the increase in the crystallization rate of the *s*PMP. As evidenced by the appearance of $(200)_{PLLA}$/$(110)_{PLLA}$ reflections (Figure S5c) and the gradual increase in the value of $X_{r,PLLA}$ (Figure S6a), the PLLA crystallization event occurred after 4 min at 110 °C, which is behind the complete crystallization of *s*PMP (3 min). The 1D SAXS profiles also remained unchanged after isothermal crystallization for 2 min, indicating that the subsequent PLLA crystallization was still confined within the crystalline *s*PMP lamellae. Similar to the behavior after isothermal crystallization at 90 °C, crystallization-induced thickening of the *s*PMP microdomain was also evident for the *s*PMP–PLLA BCP crystallized at 110 °C (Figure S6b). In addition, significant chain stretching of the PLLA was also induced by the first-crystallized *s*PMP, thereby increasing the microdomain thicknesses of the PLLA. As calculated, the long period of the *s*PMP–PLLA BCP crystallized isothermally at 110 °C for 2 min was 38.5 nm—a large increase of 34% relative to the value for the amorphous lamellae (ca. 28.8 nm at t = 0 min). We attribute this behavior to the greater crystalline thickness of the *s*PMP crystallized at higher temperature, giving rise to a dramatic decrease in the junction distance. The lamellar long periods varied with crystallization temperatures are shown in Figure 9. Before crystallization, the long periods gradually decrease with the increase of the crystallization temperature due to the decrease of the BCP segregation strength. After crystallization, the long periods increase with the

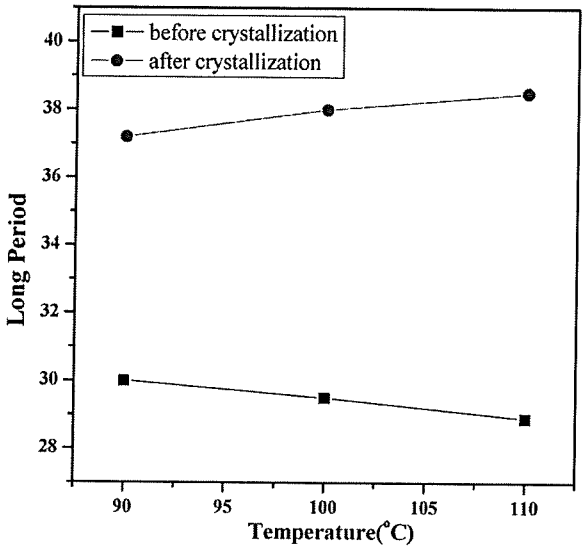

Figure 9. Long periods of the *s*PMP–PLLA BCP before and after crystallization at various temperatures.

increase of temperature due to the increase of the crystalline thickness. Accordingly, highly elongated lamellar long periods from 24% to 34% can be obtained with the elevation of crystallization temperature from 90 to 110 °C. Consequently, the switchable lamellar nanostructures with significant dimensional change can be carried out by simply controlling crystallization or melting of the crystallizable blocks.

Crystalline Orientation in the Lamellar Nanostructures. To examine the crystallographic details for the chain orientation of the *s*PMP and PLLA in the *s*PMP–PLLA after crystallization, well-oriented lamellar nanostructures were carried out by oscillatory shear. Figure 10 shows the 2D

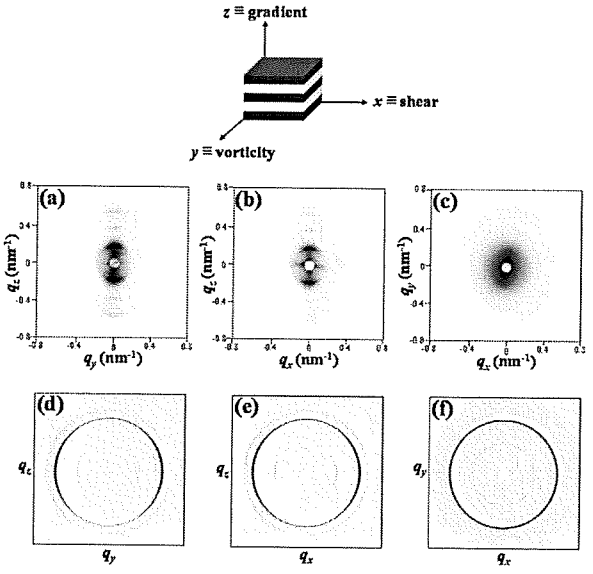

Figure 10. 2D SAXS patterns of the shear-aligned *s*PMP–PLLA after crystallization at 110 °C for 3 h along (a) x, (b) y, and (c) z directions. The corresponding 2D WAXD patterns along (d) x, (e) y, and (f) z directions.

dx.doi.org/10.1021/jp504976s | J. Phys. Chem. C 2014, 118, 19402–19414

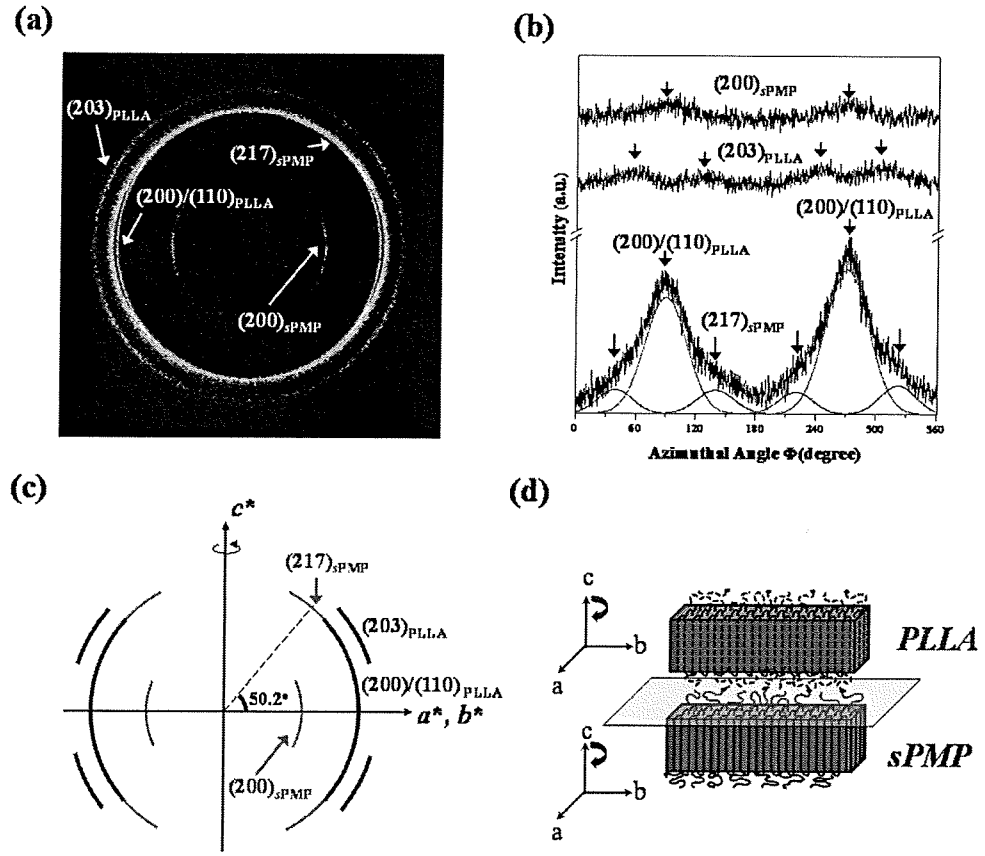

Figure 11. (a) 2D WAXD pattern and (b) the corresponding azimuthal profiles of the shear-aligned *s*PMP–PLLA crystallized at 110 °C along the *x* direction. (c) Schematic illustration of the coexistence of $[00l]_{PLLA}$ and $[00l]_{sPMP}$ uniaxial patterns. (d) Schematic illustration of the homeotropic orientation of the *s*PMP and PLLA crystals within the lamellar nanostructure.

SAXS patterns for the shear-aligned *s*PMP–PLLA after crystallization at T_c = 110 °C. As illustrated, shear, vorticity, and velocity gradient directions are denoted as *x*, *y*, and *z*, respectively. As shown, strong anisotropic reflections with the relative q^* ratios of 1:2:3 along meridian direction can be observed in the 2D SAXS patterns along *x* and *y* directions (Figures 10a and 10b). By contrast, an unstructured pattern is obtained along the *z* direction (Figure 10c). Consequently, well-oriented lamellar nanostructures can be preserved in the shear-aligned *s*PMP–PLLA after crystallization at T_c = 110 °C.

Similar to the 2D SAXS results, the corresponding 2D WAXD patterns display significant anisotropic reflections along *x* and *y* directions (Figures 10d and 10e), whereas an isotropic ring pattern along the *z* direction is observed (Figure 10f). Apparently, this reveals that the *s*PMP and PLLA crystals might form a specific crystalline orientation within the lamellar nanostructures. On the basis of the pseudo-orthorhombic lattice structure of the α-form PLLA crystal (a = 1.06 nm, b = 0.61 nm, c = 2.88 nm, and $\alpha = \beta = \gamma = 90°$),[65,66] two intense arcs on the equator correspond to the $(200)_{PLLA}/(110)_{PLLA}$ reflections or vice versa because of the equal interplane distance ($d_{(200)}^{PLLA} \sim d_{(110)}^{PLLA}$ = 0.53 nm) (Figure 11a). Four outer off-axis arcs result from the $(203)_{PLLA}$ reflections. Also, according to the tetragonal lattice structure of the *s*PMP crystal (a = 1.8 nm, b = 1.8 nm, c = 4.69 nm, and $\alpha = \beta = \gamma = 90°$),[60,67] two anisotropic $(200)_{sPMP}$ reflections along equatorial direction can be found in the inner region. Notably, the $(200)_{PLLA}/(110)_{PLLA}$ reflections exhibit an unusual diffused arcs in intensity. We suggest that this might be associated with the overlapping of the $(217)_{sPMP}$ and the $(200)_{PLLA}/(110)_{PLLA}$ reflections due to the similar interplane distance ($d_{(200)}^{PLLA} \sim d_{(110)}^{PLLA}$ = 0.57 nm, $d_{(217)}^{sPMP}$ = 0.52 nm). Therefore, the azimuthal scan for the corresponding 2D WAXD pattern was conducted for detailed analysis (Figure 11b). As shown, four $(203)_{PLLA}$ peaks are found at the azimuthal angles Φ = 60°, 120°, 240°, and 300°; two $(200)_{sPMP}$ peaks are obtained at Φ = 90° and 270°. Two broad $(200)_{PLLA}/(110)_{PLLA}$ peaks at Φ = 90° and 270° can be found, suggesting the overlapping of the $(217)_{sPMP}$ reflections. After peak deconvolution, four $(217)_{sPMP}$ peaks can be found at Φ = 40°, 140°, 221°, and 322°. As calculated, in the typical fiber pattern along the *c*-axis for the *s*PMP crystal (i.e., [00l] uniaxial pattern), the $(217)_{sPMP}$ reflections can be obtained at Φ = 39.8°, 140.2°, 219.8°, and 320.8°, consistent with the azimuthal profile after peak deconvolution. According to the corresponding features, the diffraction patterns at T_c = 110 °C suggest the coexistence of two sets of uniaxial patterns, that is, the $[001]_{PLLA}$ and $[001]_{sPMP}$ uniaxial patterns as illustrated in Figure 11c. Consequently, after crystallization at T_c = 110 °C, both *c*-axes of the PLLA and *s*PMP crystals are parallel to the normal of the lamellar nanostructure (i.e., the homeotropic orientation) in the *s*PMP–PLLA (Figure 11d). This is in line with the previous suggestion that the dense packing of the *s*PMP crystal may lead to the shrinkage of the junction distance. Consistently, the homeotropic orientations are found for the

dx.doi.org/10.1021/jp504976s | J. Phys. Chem. C 2014, 118, 19402–19414

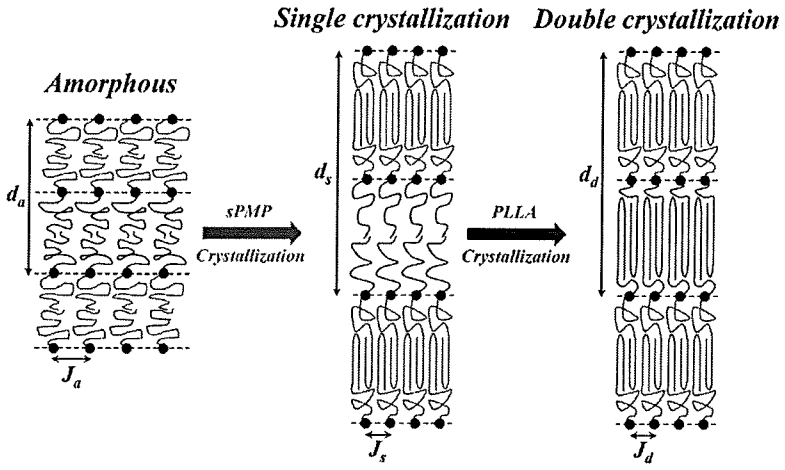

Figure 12. Schematic representation of the self-assembled morphologies—amorphous, single-crystalline, and double-crystalline lamellae—formed by the *s*PMP–PLLA BCP during the crystallization sequence.

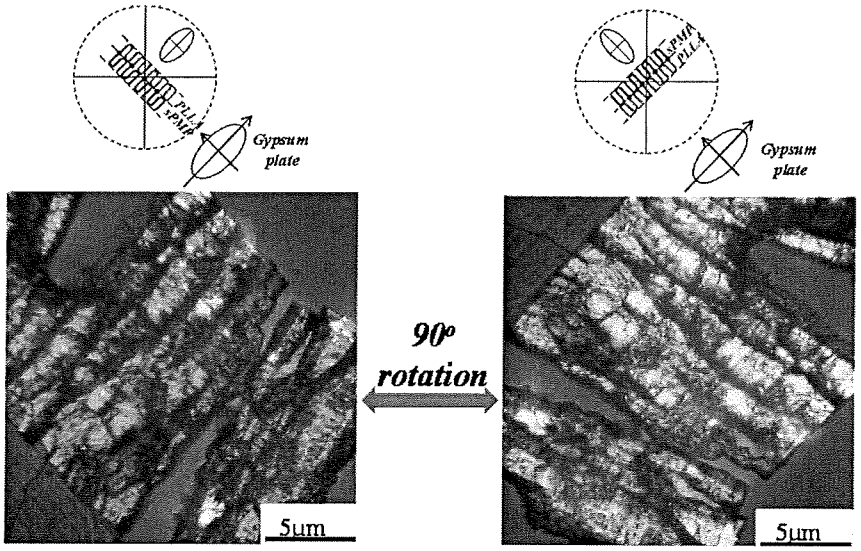

Figure 13. PLM photographs for the shear-aligned *s*PMP–PLLA after double crystallization at 110 °C.

*s*PMP–PLLA crystallized at T_c = 90, 100, and 120 °C (Figures S7–S9). As a result, both *s*PMP and PLLA crystals display the homeotropic orientation within the lamellar nanostructure in the *s*PMP–PLLA at T_c = 80–120 °C.

Figure 12 displays a schematic representation of the dimensional changes for self-assembled morphologies—amorphous, single-crystalline, and double-crystalline lamellae—formed by the *s*PMP–PLLA BCP during the crystallization sequence. Prior to crystallization, the *s*PMP and PLLA chains both exhibited coiled chain conformations (i.e., larger entropy) to compensate for the enthalpy contribution from the large interfacial area (or junction distance). After the *s*PMP blocks crystallize first (i.e., single crystallization), the lamellar morphology is preserved as a result of the strong segregation of the *s*PMP–PLLA BCP. Because of the dense packing of the *s*PMP crystals with homeotropic orientation, shrinkage of the junction distance from J_a to J_s is expected, resulting in stretching of the *s*PMP and PLLA chains. Meanwhile, this may cause the large increase of the long period in the *s*PMP–PLLA BCP. Accordingly, a phase transition occurred from the amorphous microphase-separated lamellae to the *s*PMP crystalline lamellae with an accompanying increase in the long period from d_a (i.e., the long period of the amorphous lamellae) to d_s (the long period of the single-crystalline lamellae)—in other words, crystallization-induced thickening of microdomains. As calculated, the cross-sectional area per junction point was reduced from 2.33 to 1.97 nm^2 as the *s*PMP block crystallized at 90 °C. In contrast, it was further reduced from 2.47 to 1.85 nm^2 as the *s*PMP block crystallized at 110 °C. Also, the number of folds per *s*PMP block chain was estimated to 2 and 1.8 for 90 and 110 °C, respectively. These results indicate that increasing crystallization temperature indeed reduces the junction distance significantly, resulting in the high degree of chain stretching. After double crystallization, the PLLA crystals also exhibited a homeotropic orientation, with the value of d_d (the long period of the double-crystalline lamellae) being almost identical to the value of d_s, due to robust confinement by the *s*PMP crystalline lamellae. The robust confinement by the *s*PMP crystalline

dx.doi.org/10.1021/jp504976s | J. Phys. Chem. C 2014, 118, 19402–19414

lamellae did indeed result in a lamellar morphology with fixed dimensions after double crystallization in the *s*PMP–PLLA BCP.

Figure 13 shows the PLM photographs of the shear-aligned *s*PMP–PLLA after double crystallization at 110 °C. As shown, the uniform birefringence from blue to yellow can be found by rotating the shear-aligned sample for 90°. This is attributed to the change of the *c*-axes of the *s*PMP and PLLA crystals from parallel to perpendicular orientation with respect to the slow direction of the gypsum plate (long axis of the ellipsoid). This observed uniform birefringence further confirms the formation of the large-area double-crystalline lamellar nanostructures with the homeotropic orientation for both *s*PMP and PLLA blocks. Also, this birefringence exhibits a reversible process through remelt and recrystallization processes, implying that the lamellar disorientation is insignificant due to the strong segregation of the *s*PMP–PLLA. As a result, the double-crystalline lamellar nanostructures with uniform birefringence and high degree of chain stretching can be carried out in the *s*PMP–PLLA BCP after double crystallization.

CONCLUSIONS

The nanostructural dimension of the double-crystalline *s*PMP–PLLA BCP featuring a lamellar phase is mainly determined by the microphase separation and the crystallization sequence. Instead of forming a breakout morphology, we observed a phase transition from the amorphous microphase-separated lamellae to the crystalline *s*PMP lamellae after the first-crystallized *s*PMP crystallization event under soft confinement, due to the strong segregation of the *s*PMP–PLLA BCP. Most interestingly, the first-crystallized *s*PMP may give rise to significant chain stretching of the PLLA, thereby increasing the microdomain thickness of the PLLA. With increasing crystallization temperature, this chain stretching may become more significant, resulting in a large increase of the lamellar long period. Because subsequent PLLA crystallization is confined strongly by the crystalline *s*PMP lamellae, a lamellar morphology with fixed dimensions was observed after double crystallization. Consequently, the double-crystalline lamellar morphology having homeotropic orientation for both *s*PMP and PLLA crystals can be obtained in the shear-aligned *s*PMP–PLLA after double crystallization, which can be verified by the uniform birefringence under PLM observation. This uniform birefringence also exhibits the thermal reversibility through the remelt and recrystallization processes. This may provide a facile process to control the dimension and optical properties of nanomaterials through crystallization, which is promising in the potential practical applications of switchable birefringence thin films for display industry and nanomechanics.

ASSOCIATED CONTENT

Supporting Information

Long periods and microdomain thicknesses of the *s*PMP and PLLA homopolymers after crystallization; high magnification of the DSC heating profiles for (a) PLLA and (b) *s*PMP homopolymers at a rate of 10 °C/min; PLM photograph for the *s*PMP–PLLA after crystallization at 90 °C for 3 min; PLM photograph for the *s*PMP–PLLA after crystallization at 90 °C for 60 min; SAXS profiles of the (a) *s*PMP and PLLA homopolymers after crystallization at 90 and 110 °C; time-resolved (a) SAXS, (b) 1D SAXS, and (c) WAXD profiles of the *s*PMP–PLLA BCP crystallized isothermally at 110 °C; (a) relative crystallinity of the respective *s*PMP and PLLA blocks plotted with respect to the isothermal annealing time, determined from time-resolved WAXD profiles recorded at T_c = 110 °C; (b) time-dependent long periods and respective microdomain thicknesses of the *s*PMP and PLLA blocks, determined from time-resolved SAXS profiles recorded at T_c = 110 °C; 2D SAXS patterns of the shear-aligned *s*PMP–PLLA after crystallization at 90, 100, and 120 °C along (a) x and (b) z directions; corresponding 2D WAXD patterns along (c) x and (d) z directions. This material is available free of charge via the Internet at http://pubs.acs.org.

AUTHOR INFORMATION

Corresponding Author

*E-mail ywchiang@mail.nsysu.edu.tw; Tel +886-7-5252000 ext 4081; Fax +886-7-5254099 (Y.W.C.).

Notes

The authors declare no competing financial interest.

ACKNOWLEDGMENTS

Authors thank Mr. Hsien-Tsan Lin of Regional Instruments Center at National Sun Yat-Sen University for his help in TEM experiments. We also thank Dr. Edwin L. Thomas of Department of Mechanical Engineering and Materials Science of University of Rice for his helpful discussions. Finally, authors appreciate the Ministry of Science and Technology (MOST 103-2221-E-110-081), Taiwan, for financially supporting this research.

REFERENCES

(1) Bates, F. S.; Fredrickson, G. H. Block Copolymer Thermodynamics: Theory and Experiment. *Annu. Rev. Phys. Chem.* **1990**, *41*, 525–557.

(2) Park, C.; Yoon, J.; Thomas, E. L. Enabling Nanotechnology with Self Assembled Block Copolymer Patterns. *Polymer* **2003**, *44*, 6725–6760.

(3) Loo, Y. L.; Register, R. A.; Adamson, D. H. Polyethylene Crystal Orientation Induced by Block Copolymer Cylinders. *Macromolecules* **2000**, *33*, 8361–8366.

(4) Loo, Y. L.; Register, R. A.; Ryan, A. J. Polymer Crystallization in 25-nm Spheres. *Phys. Rev. Lett.* **2000**, *84*, 4120–4123.

(5) Loo, Y. L.; Register, R. A.; Ryan, A. J.; Dee, G. T. Polymer Crystallization Confined in One, Two, or Three Dimensions. *Macromolecules* **2001**, *34*, 8968–8977.

(6) Loo, Y. L.; Register, R. A.; Ryan, A. J. Modes of Crystallization in Block Copolymer Microdomains: Breakout, Templated, and Confined. *Macromolecules* **2002**, *35*, 2365–2374.

(7) Zhu, L.; Cheng, S. Z. D.; Calhoun, B. H.; Ge, Q.; Quirk, R. P.; Thomas, E. L.; Hsiao, B. S.; Yeh, F.; Lotz, B. Crystallization Temperature-Dependent Crystal Orientations within Nanoscale Confined Lamellae of a Self-Assembled Crystalline–Amorphous Diblock Copolymer. *J. Am. Chem. Soc.* **2000**, *122*, 5957–5967.

(8) Zhu, L.; Calhoun, B. H.; Ge, Q.; Quirk, R. P.; Cheng, S. Z. D.; Thomas, E. L.; Hsiao, B. S.; Yeh, F.; Liu, L. Z.; Lotz, B. Initial-Stage Growth Controlled Crystal Orientations in Nanoconfined Lamellae of a Self-Assembled Crystalline–Amorphous Diblock Copolymer. *Macromolecules* **2001**, *34*, 1244–1251.

(9) Zhu, L.; Cheng, S. Z. D.; Huang, P.; Ge, Q.; Quirk, R. P.; Thomas, E. L.; Lotz, B.; Hsiao, B. S.; Yeh, F.; Liu, L. Z. Nanoconfined Polymer Crystallization in the Hexagonally Perforated Layers of a Self-Assembled PS-*b*-PEO Diblock Copolymer. *Adv. Mater.* **2002**, *14*, 31–34.

(10) Huang, P.; Zhu, L.; Guo, Y.; Ge, Q.; Jing, A. J.; Chen, W. Y.; Quirk, R. P.; Cheng, S. Z. D.; Thomas, E. L.; Lotz, B.; et al. Confinement Size Effect on Crystal Orientation Changes of Poly(ethylene oxide) Blocks in Poly(ethylene oxide)-*b*-polystyrene Diblock Copolymers. *Macromolecules* **2004**, *37*, 3689–3698.

(11) Ho, R. M.; Lin, F. H.; Tsai, C. C.; Lin, C. C.; Ko, B. T.; Hsiao, B. S.; Sics, I. Crystallization-Induced Undulated Morphology in Polystyrene-*b*-Poly(L-lactide) Block Copolymer. *Macromolecules* **2004**, *37*, 5985−5994.
(12) Ho, R. M.; Chiang, Y. W.; Lin, C. C.; Huang, B. H. Crystallization and Melting Behavior of Poly(ε-caprolactone) under Physical Confinement. *Macromolecules* **2005**, *38*, 4769−4779.
(13) Ho, R. M.; Chung, T. M.; Tsai, J. C.; Kuo, J. C.; Hsiao, B. S.; Sics, I. Crystallization of Polystyrene-*block*-[Syndiotactic Poly(propylene)] Block Copolymers from Confinement to Breakout. *Macromol. Rapid Commun.* **2005**, *26*, 107−111.
(14) Chiang, Y. W.; Ho, R. M.; Ko, B. T.; Lin, C. C. Springlike Nanohelical Structures in Chiral Block Copolymers. *Angew. Chem., Int. Ed.* **2005**, *44*, 7969−7972.
(15) Sun, Y. S.; Chung, T. M.; Li, Y. J.; Ho, R. M.; Ko, B. T.; Jeng, U. S.; Lotz, B. Crystalline Polymers in Nanoscale 1D Spatial Confinement. *Macromolecules* **2006**, *39*, 5782−5788.
(16) Chiang, Y. W.; Ho, R. M.; Thomas, E. L.; Burger, C.; Hsiao, B. S. A Spring-Like Behavior of Chiral Block Copolymer with Helical Nanostructure Driven by Crystallization. *Adv. Funct. Mater.* **2009**, *19*, 448−459.
(17) Chung, T. M.; Wang, T. C.; Ho, R. M.; Sun, Y. S.; Ko, B. T. Polymeric Crystallization under Nanoscale 2D Spatial Confinement. *Macromolecules* **2010**, *43*, 6237−6240.
(18) Douzinas, K. C.; Cohen, R. E.; Halasa, A. F. Evaluation of Domain Spacing Scaling Laws for Semicrystalline Diblock Copolymers. *Macromolecules* **1991**, *24*, 4457−4459.
(19) Douzinas, K. C.; Cohen, R. E. Chain Folding in EBEE Semicrystalline Diblock Copolymers. *Macromolecules* **1992**, *25*, 5030−5035.
(20) Cohen, R. E.; Bellare, A.; Drzewinski, M. A. Spatial Organization of Polymer Chains in A Crystallizable Diblock Copolymer of Polyethylene and Polystyrene. *Macromolecules* **1994**, *27*, 2321−2323.
(21) Ryan, A. J.; Hamley, I. W.; Bras, W.; Bates, F. S. Structure Development in Semicrystalline Diblock Copolymers Crystallizing from the Ordered Melt. *Macromolecules* **1995**, *28*, 3860−3868.
(22) Hamley, I. W.; Fairclough, J. P. A.; Terrill, N. J.; Ryan, A. J.; Lipic, P. M.; Bates, F. S.; Towns-Andrews, E. Crystallization in Oriented Semicrystalline Diblock Copolymers. *Macromolecules* **1996**, *29*, 8835−8843.
(23) Koo, C. M.; Wu, L. F.; Lim, L. S.; Mahanthappa, M. K.; Hillmyer, M. A.; Bates, F. S. Microstructure and Mechanical Properties of Semicrystalline−Rubbery−Semicrystalline Triblock Copolymers. *Macromolecules* **2005**, *38*, 6090−6098.
(24) Chen, H. L.; Hsiao, S. C.; Lin, T. L.; Yamauchi, K.; Hasegawa, H.; Hashimoto, T. Microdomain-Tailored Crystallization Kinetics of Block Copolymers. *Macromolecules* **2001**, *34*, 671−674.
(25) Zhu, L.; Cheng, S. Z. D.; Calhoun, B. H.; Ge, Q.; Quirk, R. P.; Thomas, E. L.; Hsiao, B. S.; Yeh, F.; Lotz, B. Phase Structures and Morphologies Determined by Self-Organization, Vitrification, and Crystallization: Confined Crystallization in an Ordered Lamellar Phase of PEO-*b*-PS Diblock Copolymer. *Polymer* **2001**, *42*, 5829−5839.
(26) Reiter, G.; Castelein, G.; Hoerner, P.; Riess, G.; Blumen, A.; Sommer, J. U. Nanometer-Scale Surface Patterns with Long-Range Order Created by Crystallization of Diblock Copolymers. *Phys. Rev. Lett.* **1999**, *83*, 3844−3847.
(27) Reiter, G.; Castelein, G.; Sommer, J. U.; Röttele, A.; Thurn-Albrecht, T. Direct Visualization of Random Crystallization and Melting in Arrays of Nanometer-Size Polymer Crystals. *Phys. Rev. Lett.* **2001**, *87*, 226101−1−226101−4.
(28) Müller, A. J.; Balsamo, V.; Arnal, M. L. In *Lecture Notes in Physics: Progress in Understanding of Polymer Crystallization*; Reiter, G., Strobl, G., Eds.; Springer: Berlin, 2007; Vol. *714*, pp 229−259.
(29) Castillo, R. V.; Müller, A. J. Crystallization and Morphology of Biodegradable or Biostable Single and Double Crystalline Block Copolymers. *Prog. Polym. Sci.* **2009**, *34*, 516−560.
(30) Kim, K. S.; Chung, S.; Chin, I. J.; Kim, M. N.; Yoon, J. S. Crystallization Behavior of Biodegradable Amphiphilic Poly(ethylene glycol)-Poly(L-lactide) Block Copolymers. *J. Appl. Polym. Sci.* **1999**, *72*, 341−348.
(31) Maglio, G.; Migliozzi, A.; Palumbo, R. Thermal Properties of Di- and Triblock Copolymers of Ppoly(L-lactide) with Poly(oxyethylene) or Poly(ε-caprolactone). *Polymer* **2003**, *44*, 369−375.
(32) Sun, L.; Liu, Y.; Zhu, L.; Hsiao, B. S.; Avila-Orta, C. A. Self-Assembly and Crystallization Behavior of a Double-Crystalline Polyethylene-*block*-Poly(ethylene oxide) Diblock Copolymer. *Polymer* **2004**, *45*, 8181−8193.
(33) Nojima, S.; Akutsu, Y.; Washino, A.; Tanimoto, S. Morphology of Melt-Quenched Poly(ε-caprolactone)-*block*-Polyethylene Copolymers. *Polymer* **2004**, *45*, 7317−7324.
(34) Nojima, S.; Akutsu, Y.; Akaba, M.; Tanimoto, S. Crystallization Behavior of Poly(ε-caprolactone) Blocks Starting from Polyethylene Lamellar Morphology in Poly(ε-caprolactone)-*block*-Polyethylene Copolymers. *Polymer* **2005**, *46*, 4060−4067.
(35) Hamley, I. W.; Castelletto, V.; Castillo, R. V.; Müller, A. J.; Martin, C. M.; Pollet, E.; Dubois, P. Crystallization in Poly(L-lactide)-*b*-poly(ε-caprolactone) Double Crystalline Diblock Copolymers: A Study Using X-ray Scattering, Differential Scanning Calorimetry, and Polarized Optical Microscopy. *Macromolecules* **2005**, *38*, 463−472.
(36) Castillo, R. V.; Arnal, M. L.; Müller, A. J.; Hamley, I. W.; Castelletto, V.; Schmalz, H.; Abetz, V. Fractionated Crystallization and Fractionated Melting of Confined PEO Microdomains in PB-*b*-PEO and PE-*b*-PEO Diblock Copolymers. *Macromolecules* **2008**, *41*, 879−889.
(37) Nojima, S.; Kiji, T.; Ohguma, Y. Characteristic Melting Behavior of Double Crystalline Poly(ε-caprolactone)-*block*-polyethylene Copolymers. *Macromolecules* **2007**, *40*, 7566−7572.
(38) Weiyu, C.; Tashiro, K.; Hanesaka, M.; Takeda, S.; Masunaga, H.; Sasaki, S.; Takata, M. Relationship between Morphological Change and Crystalline Phase Transitions of Polyethylene-Poly(ethylene Oxide) Diblock Copolymers, Revealed by the Temperature-dependent Synchrotron WAXD/SAXS and Infrared/Raman Spectral Measurements. *J. Phys. Chem. B* **2009**, *113*, 2338−2346.
(39) Castillo, R. V.; Müller, A. J.; Raquez, J. M.; Dubois, P. Crystallization Kinetics and Morphology of Biodegradable Double Crystalline PLLA-*b*-PCL Diblock Copolymers. *Macromolecules* **2010**, *43*, 4149−4160.
(40) Cong, Y. H.; Liu, H.; Wang, D. L.; Zhao, B. J.; Yan, T. Z.; Li, L. B.; Chen, W.; Zhong, Z. Y.; Lin, M. C.; Chen, H. L.; et al. Stretch-Induced Crystallization through Single Molecular Force Generating Mechanism. *Macromolecules* **2011**, *44*, 5878−5882.
(41) Li, S.; Myers, S. B.; Register, R. A. Solid-State Structure and Crystallization in Double-Crystalline Diblock Copolymers of Linear Polyethylene and Hydrogenated Polynorbornene. *Macromolecules* **2011**, *44*, 8835−8844.
(42) Yang, J. J.; Liang, Y. R.; Luo, J.; Zhao, C. Z.; Han, C. C. Multilength Scale Studies of the Confined Crystallization in Poly(L-lactide)-*block*-Poly(ethylene glycol) Copolymer. *Macromolecules* **2012**, *45*, 4254−4261.
(43) Lin, M. C.; Chen, H. L.; Su, W. B.; Su, C. J.; Jeng, U. S.; Tzeng, F. Y.; Wu, J. Y.; Tsai, J. C.; Hashimoto, T. Interactive Crystallization Kinetics in Double-Crystalline Block Copolymer. *Macromolecules* **2012**, *45*, 5114−5127.
(44) Nojima, S.; Ono, M.; Ashida, T. Crystallization of Block Copolymers II. Morphological Study of Poly(ethylene glycol)-Poly(ε-caprolactone) Block Copolymers. *Polym. J.* **1992**, *24*, 1271−1280.
(45) Gan, Z. H.; Jiang, B. Z.; Zhang, J. Poly(ε-caprolactone)/Poly(ethylene oxide) Diblock Copolymer. I. Isothermal Crystallization and Melting Behavior. *J. Appl. Polym. Sci.* **1996**, *59*, 961−967.
(46) Bogdanov, B.; Vidts, A.; Schacht, E.; Berghmans, H. Isothermal Crystallization of Poly(ε-caprolactone-ethylene glycol) Block Copolymers. *Macromolecules* **1999**, *32*, 726−731.
(47) Shiomi, T.; Imai, K.; Takenaka, K.; Takeshita, H.; Hayashi, H.; Tezuka, Y. Appearance of Double Spherulites Like Concentric Circles for Poly(ε-caprolactone)-*block*-Poly(ethylene glycol)-*block*-Poly(ε-caprolactone). *Polymer* **2001**, *42*, 3233−3239.

(48) Albuerne, J.; Marquez, L.; Müller, A. J.; Raquez, J. M.; Degée, P.; Dubois, P.; Castelletto, V.; Hamley, I. W. Nucleation and Crystallization in Double Crystalline Poly(*p*-dioxanone)-*b*-poly(*ε*-caprolactone) Diblock Copolymers. *Macromolecules* **2003**, *36*, 1633–1644.

(49) Takeshita, H.; Fukumoto, K.; Ohnishi, T.; Ohkubo, T.; Miya, M.; Takenaka, K.; Shiomi, T. Formation of Lamellar Structure by Competition in Crystallization of Both Components for Crystalline–Crystalline Block Copolymers. *Polymer* **2006**, *47*, 8210–8218.

(50) Nojima, S.; Fukagawa, Y.; Ikeda, H. Interactive Crystallization of a Strongly Segregated Double Crystalline Block Copolymer with Close Crystallizable Temperatures. *Macromolecules* **2009**, *42*, 9515–9522.

(51) Castillo, R. V.; Müller, A. J.; Lin, M. C.; Chen, H. L.; Jeng, U. S.; Hillmyer, M. A. Confined Crystallization and Morphology of Melt Segregated PLLA-*b*-PE and PLDA-*b*-PE Diblock Copolymers. *Macromolecules* **2008**, *41*, 6154–6164.

(52) Myers, S. B.; Register, R. A. Crystalline–Crystalline Diblock Copolymers of Linear Polyethylene and Hydrogenated Polynorbornene. *Macromolecules* **2008**, *41*, 6773–6779.

(53) Schmidt, S. C.; Hillmyer, M. A. Synthesis and Characterization of Model Polyisoprene-Polylactide Diblock Copolymers. *Macromolecules* **1999**, *32*, 4794–4801.

(54) Asanuma, T.; Nishimori, Y.; Ito, M.; Uchikawa, N.; Shiomura, T. Preparation of Syndiotactic Polyolefins by Using Metallocene Catalysts. *Polym. Bull.* **1991**, *25*, 567–570.

(55) Kuo, J. C.; Lin, W. F.; Yu, C. H.; Tsai, J. C.; Wang, T. C.; Chung, T. M.; Ho, R. M. Isotactic Polypropylene-Based Stereoregular Diblock Copolymers: Syntheses and Self-Assembly. *Macromolecules* **2008**, *41*, 7967–7977.

(56) Tzeng, F. Y.; Lin, M. C.; Wu, J. Y.; Kuo, J. C.; Tsai, J. C.; Hsiao, M. S.; Chen, H. L.; Cheng, S. Z. D. Stereoregular Diblock Copolymers of Syndiotactic Polypropylene and Polyesters: Syntheses and Self-Assembled Nanostructures. *Macromolecules* **2009**, *42*, 3073–3085.

(57) Lee, J. Y.; Shiao, M. C.; Tzeng, F. Y.; Chang, C. H.; Tsai, C. K.; Lo, K. S.; Lin, S. C.; Ho, R. M. Syndiotactic Polyallyltrimethylsilane-Based Stereoregular Diblock Copolymers: Syntheses and Self-Assembled Nanostructures. *Macromolecules* **2012**, *45*, 2720–2730.

(58) Jeng, U. S.; Su, C. H.; Su, C. J.; Liao, K. F.; Chuang, W. T.; Lai, Y. H.; Chang, J. W.; Chen, Y. J.; Huang, Y. S.; Lee, M. T.; et al. A Small/Wide-Angle X-ray Scattering Instrument for Structural Characterization of Air–Liquid Interfaces, Thin Films and Bulk Specimens. *J. Appl. Crystallogr.* **2010**, *43*, 110–121.

(59) Sakai, F.; Nishikawa, K.; Inoue, Y.; Yazawa, K. Nucleation Enhancement Effect in Poly(L-lactide) (PLLA)/Poly(*ε*-caprolactone) (PCL) Blend Induced by Locally Activated Chain Mobility Resulting from Limited Miscibility. *Macromolecules* **2009**, *42*, 8335–8342.

(60) De Rosa, C.; Venditto, V.; Guerra, G.; Corradini, P. Chain Conformation and Unit Cell in the Crystalline Phase of Syndiotactic Poly(4methyl-1-pentene). *Macromolecules* **1992**, *25*, 6938–6942.

(61) Strobl, G. R.; Schneider, M. Direct Evaluation of the Electron Density Correlation Function of Partially Crystalline Polymers. *J. Polym. Sci., Part B: Polym. Phys.* **1980**, *18*, 1343–1359.

(62) Roe, R. *Methods of X-ray and Neutron Scattering in Polymer Science*; Oxford University Press: New York, 2000; p 201.

(63) Yazici, O.; Cakar, F.; Cankurtaran, O.; Karaman, F. Determination of Dielectric Properties by Solubility Parameter of Poly(4-methyl-1-pentene). *Optoelectron. Adv. Mater., Rapid Commun.* **2008**, *2*, 655–658.

(64) Blomqvist, J.; Mannfors, B.; Pietilä, L.-O. Amorphous Cell Studies of Polyglycolic, Poly(L-lactic), Poly(L,D-lactic) and Poly(glycolic/L-lactic) Acids. *Polymer* **2002**, *43*, 4571–4583.

(65) Cartier, L.; Okihara, T.; Ikada, Y.; Tsuji, H.; Puiggali, J.; Lotz, B. Epitaxial Crystallization and Crystalline Polymorphism of Polylactides. *Polymer* **2000**, *41*, 8909–8919.

(66) Alemán, C.; Lotz, B.; Puiggali, J. Crystal Structure of the *α*-Form of Poly(L-lactide). *Macromolecules* **2001**, *34*, 4795–4801.

(67) De Rosa, C.; Venditto, V.; Guerra, G.; Corradini, P. Crystal Structure of Syndiotactic Poly(4-methyl-1-pentene). *Polymer* **1995**, *36*, 3619–3624.